

Absorption spectra of Fe L-lines in Seyfert 1 galaxies

J. Dubau^{a,*}, D. Porquet^b, O. Z. Zabaydullin^c

^a*LIXAM, Université Paris-Sud, 91405 Orsay cedex, France*

^b*SAP, CEA-Saclay, 91191 Gif-sur-Yvette, France*

^c*Institute of Nuclear Fusion, Kurchatov Institute, Moscow, Russia*

Abstract

Absorption L-lines of iron ions are observed, in absorption, in spectra of Seyfert 1 galaxies by the new generation of X-ray satellites: Chandra (NASA) and XMM-Newton (ESA). Lines associated to Fe²³⁺ to Fe¹⁷⁺ are well resolved. Whereas, those corresponding to Fe¹⁶⁺ to Fe⁶⁺ are unresolved. Forbidden transitions of the Fe¹⁶⁺ to Fe⁶⁺ ions were previously observed, for the same objects, in the visible and infra-red regions, showing that the plasma had a low density. To interpret X-ray, visible and infra-red data, astrophysical models assume an extended absorbing medium of very low density surrounding an intense X-ray source. We have calculated atomic data (wavelengths, radiative and autoionization rates) for n=2 to n'=3-4 transitions and used them to construct refined synthetic spectra of the unresolved part of the L-line spectra.

Key words: X-ray; absorption lines; atomic processes

* Corresponding author. Fax: +33-169155811

Email address: jacques.dubau@lixam.u-psud.fr (J. Dubau).

1 Introduction

The new generation of X-ray satellites (*Chandra* and *XMM-Newton*) produces very detailed spectra, thanks to a high spectral resolution combined to a high sensitivity of the spectrometers on board. For the first time, it is possible to have access to X-ray spectroscopy of extra-solar astrophysical objects: e.g., stellar coronae, Active Galactic Nuclei (AGN), X-ray binaries, etc. In particular, observations of Seyfert galaxies, show numerous lines of highly ionized elements: predominantly in absorption, for Seyfert 1 and only in emission for Seyfert 2 galaxies.

Much atomic data have already been calculated to analyze X-ray spectra of solar corona or laboratory plasmas. The well-known He-like ion diagnostics [1], [2] have been extended from solar to non-solar coronae and also to photoionized plasmas [3], [4]. Besides these K-lines, Fe-L lines have also been observed in X-ray spectra, for Seyfert 1 [5](Fig. 1), [6], [7] and for Seyfert 2 [8] (Fig.2) galaxies. To analyze the unresolved part of the Fe-L spectra (Fe^{16+} to Fe^{6+}), atomic data for the transitions from $n=2$ to $n'=3$ have been calculated and presented as an abbreviated set, assuming a UTA (unresolved transition array) statistical model [9], i.e. mean wavelengths, statistical spectral widths of transition arrays, etc. The arguments used by the authors to justify statistical treatment is that various processes, such as turbulence, will merge lines into a broad UTA, independent of the spectral resolution of the measuring device. Comparisons of the Seyfert 1 NGC 3783 spectra with different spectral resolutions (see Tables 1), XMM [6] and Chandra [7] (Fig 3), show that the statistical assumption is not justified at least for this object. In Fig. 3, finer detail can be clearly resolved. Indeed, for such a low density

plasma the number of possible absorption transitions is quite limited and as the absorption changes dramatically over the ionization stages (see Tables 2, 3) the use of a statistical width artificially increases the real width of the lines. We have therefore re-calculated all the atomic data of [9], extending them to $n'=4$ transitions, giving a particular importance to the numerous possible autoionization channels.

2 Seyfert Galaxies

Seyfert galaxies, discovered by Seyfert [10], have very compact and bright centers, the so-called Active Galactic Nuclei (AGN) : their bolometric luminosities (i.e., including all wavelength contributions) $L_{\text{bol}} \sim 10^{10}\text{-}10^{11}L_{\odot}$, L_{\odot} being the solar bolometric luminosity. The surrounding stars are relatively faint compared to the central nucleus. These galaxies are relatively close to our galaxy exhibiting small red-shifts ($z \equiv \Delta\lambda/\lambda \leq 0.05$). Seyfert galaxy optical spectra show strong emission lines of ionized gas plus a non-stellar continuum. The energy power from the galactic nucleus is commonly supposed to be due to some super-massive black hole ($M_{\text{BH}} \sim 10^6\text{-}10^9 M_{\odot}$, (where M_{\odot} is the solar mass)) surrounded by an accretion disk (see Fig. 4). This disk is observed in emission in all wavelengths from X-ray to infra-red.

There are two types of Seyfert galaxies: the Seyfert 1 and the Seyfert 2, distinguished by their observed visible spectra. The Seyfert 1 show both broad (Full Width at Half Maximum: $\text{FWHM} \sim 2\,000\text{--}20\,000 \text{ km s}^{-1}$) and narrow ($\text{FWHM} \leq 2\,000 \text{ km s}^{-1}$) lines, while Seyfert 2 exhibit only narrow lines. However, Antonucci & Miller [11], in the NGC 1068 Seyfert 2, detected also broad lines using polarimetry. This led to the conjuncture that Seyfert 1 and Seyfert

2 are the same type of objects but viewed with different angles. That is, for Seyfert 1, the observer views the central continuum source which is the “Broad Line Region” while, in Seyfert 2, the observer views the external part or the “Narrow Line Region”, due to obscuration of the central continuum source by some molecular torus (see Fig. 3). This model is supported by the discovery in the X-ray spectrum of a dilute and high ionization medium called the “Warm Absorber” (discovered by Halpern [13] in MR2251-178), mainly observed in absorption in Seyfert 1, while only seen in emission in Seyfert 2 (e.g., Kinkhabwala et al.[8]).

3 Calculations of atomic parameters

3.1 Method

Wavelengths λ , oscillator strengths f and radiative transition probabilities A_r have been calculated using the SUPERSTRUCTURE code developed at UC London [14], which uses a multi-configuration expansion of the wave functions. The atomic Hamiltonian includes most of the Breit Pauli relativistic corrections (one-body and two-body terms). The non-relativistic and relativistic eigenstates are obtained by diagonalizing the Schrödinger and Breit Pauli Hamiltonian respectively. The matrix transformation between both eigenstates is then used to transform non-relativistic autoionization transition matrix elements to fine-structure autoionization probabilities A_a , in the AUTOLSJ code [15]. The radial parts of the one electron wave-functions are calculated in scaled Thomas-Fermi-Dirac potentials, the scaling parameters, for each l orbital, being derived by minimizing the energies of some selected

LS terms.

3.2 Results

Calculations have been done for 11 ions from Fe^{+16} to Fe^{+6} using the ground state configuration and the excited configurations accessible by absorption (i.e., by electric-dipole transitions). For example:

Fe^{+16} : $1s^2 2s^2 2p^6$, $1s^2 2s^2 2p^5 3s$, $1s^2 2s^2 2p^5 3d$, $1s^2 2s 2p^6 3p$, $1s^2 2s^2 2p^5 4s$, $1s^2 2s^2 2p^5 4d$,
 $1s^2 2s 2p^6 4p$

and

Fe^{+6} : $1s^2 2s^2 2p^6 3s^2 3p^6 3d^2$, $1s^2 2s^2 2p^5 3s^2 3p^6 3d^3$, $1s^2 2s^2 2p^5 3s^2 3p^6 3d^2 4s$, $1s^2 2s^2 2p^5 3s^2 3p^6 3d^2 4d$,
 $1s^2 2s 2p^6 3s^2 3p^6 3d^2 4p$.

For Fe^{+16} , the excited configurations give bound states. Whereas for Fe^{+15} to Fe^{+6} , the excited configurations correspond to autoionizing states. As examples we provide in Tables 2, 3, the wavelengths, absorption oscillator strengths, radiative and autoionization probabilities for Fe^{+15} , Fe^{+14} and Fe^{+8} . One can observe the dramatic increase in the autoionization probabilities from Fe^{+15} to Fe^{+8} . Moreover, the number of possible autoionizing channels increases also dramatically. This, in particular, explains why one does not observe the emission lines in Seyfert 2 which could correspond to the absorption lines in Seyfert 1 (see Fig. 2). That is, for L-lines, the photo-excited bound states, Fe^{+23} to Fe^{+16} , decay by the reverse radiative transition whereas the photo-excited autoionizing states, Fe^{+15} to Fe^{+6} , decay preferentially by autoionization.

4 Synthetic spectral modeling for the iron inner-shell photo-excitation lines

The optical depth $\tau_{ij}(\nu)$ due to an absorption line ($i \rightarrow j$) can be written as

$$\tau_{ij}(\nu) = N_{ion} \times \sigma_{ij}(\nu)$$

where N_{ion} is the ionic column density along the line of sight to the source (in cm^{-2}) and $\sigma_{ij}(\nu)$ is the photo-excitation cross-section from i to j .

The photo-excitation (or photo-absorption) cross-section is:

$$\sigma_{ij}(\nu) = \frac{\pi e^2}{m_e c} f_{ij} \phi(\nu) \phi(\nu), \quad (1)$$

where e and m_e are the electron charge and mass, c is the speed of light, f_{ij} the absorption oscillator strength, and $\phi(\nu)$ is a normalized line profile.

In Fig 5, the relative photo-absorption cross-sections of Fe^{+16} to Fe^{+6} are presented with the normalization factor being the same for each graph. If instrumental width is the dominant broadening process of the lines, the same gaussian profile can be used for all lines. The graph in the lower right is the sum of all the contributions with the assumption that each ion has the same abundance.

5 Conclusion

The new generation of X-ray satellites (*Chandra* and *XMM-Newton*) provide us with higher resolution spectra than was previously available. For the first time, we have access to high resolution X-ray spectroscopy of non-solar objects.

In particular, observations of Seyfert 1 galaxies, show very complex spectra with the presence of numerous absorption lines. Accurate atomic data are crucial to infer most of the physical and geometrical parameters of the “Warm Absorber”. We have calculated complete atomic data sets (wavelength, oscillator strength, auto-ionization rates) for inner-shell $n=2-3$ and $n=2-4$ (mainly $2p-3d$, $2p-4d$) photo-excitation for Fe ions (from 10 electrons to 20 electrons). Observations in UV, visible and infra-red wavelengths, where those Fe ions emit the most, are also important to have a realistic plasma modeling.

References

- [1] Gabriel AH, Jordan C MNRAS 1969;145:241.
- [2] Bely-Dubau F, Dubau J, Faucher P, Gabriel AH MNRAS 1982;198:239.
- [3] Porquet D, Dubau J A&AS 2000;143:495.
- [4] Porquet D, Mewe R, Dubau J, Raassen AJJ, Kaastra JS A&A 2001;376:1132.
- [5] Sako M, Kahn SM, Behar E, Kaastra JS, et al. A&A 2001;365:L168.
- [6] Blustin AJ, Branduardi-Raymont G, Behar E, et al. KC A&A 2002;392:453.
- [7] Kaspi S, Brandt WN, George IM, et al. ApJ 2002;574:643.
- [8] Kinkhabwala A., Sako M., Behar E. et al. ApJ 2002;575:732.
- [9] Behar E, Sako M, Kahn SM ApJ 2001;563:497.
- [10] Seyfert CK ApJ 1943;97:28.
- [11] Antonucci RRJ, Miller JS. ApJ 1985;297:621.
- [12] Urry CM, Padovani P PASP 1995;107:803.

- [13] Halpern JP ApJ 1984;281:90.
- [14] Eissner W, Jones M, Nussbaumer H Comp Phys Commun 1974;8:270.
- [15] TFR Group, Dubau J, Loulergue M J Phys B 1981;15:1007.

Table 1

Energy (keV) and wavelength (\AA) ranges, as well as the spectral resolution of the spectrometers aboard the new generation of X-ray satellites: *Chandra* (NASA) and *XMM-Newton* (ESA). The *LETG* and the *HETG* are onboard *Chandra*, and the *RGS* is on board *XMM-Newton*.

	<i>LETG</i>	<i>HETG</i>	<i>RGS</i>
E (keV)	[0.07 – 8.86]	[0.4 – 10.0]	[0.35 – 2.5]
λ (\AA)	[1.4 – 170]	[1.2 – 31]	[5 – 38]
$\Delta\lambda$ (\AA)	0.05	0.012-0.023	0.06

Table 2

Absorption oscillator strengths, wavelengths, radiative and autoionization probabilities

(from the ground level of Fe ¹⁵⁺) $1s^2 2s^2 2p^6 3s^2 S_{1/2}$				
to the upper level	f (abs)	A _r (s ⁻¹)	λ(Å)	A _a (s ⁻¹)
$1s^2 2s^2 2p^5 3s^2 \ ^2P_{3/2}$	0.07	7.96 (+11)	17.20	8.50 (+12)
$1s^2 2s^2 2p^5 3s^2 \ ^2P_{1/2}$	0.04	8.76 (+11)	16.92	8.71 (+12)
$1s^2 2s^2 2p^5 3s 3d \ ^2P_{3/2}$	0.06	8.74 (+11)	15.44	1.95 (+12)
$1s^2 2s^2 2p^5 3s 3d \ ^4D_{1/2}$	0.12	3.47 (+12)	15.36	7.46 (+05)
$1s^2 2s^2 2p^5 3s 3d \ ^4D_{3/2}$	0.22	3.08 (+12)	15.34	4.04 (+10)
$1s^2 2s^2 2p^5 3s 3d \ ^2D_{3/2}$	0.35	5.03 (+12)	15.20	2.13 (+12)
$1s^2 2s^2 2p^5 3s 3d \ ^2P_{1/2}$	0.94	2.75 (+13)	15.09	4.40 (+12)
$1s^2 2s^2 2p^5 3s 3d \ ^2P_{3/2}$	1.50	2.20 (+13)	15.07	1.82 (+12)
$1s^2 2s 2p^6 3s 3p \ ^2P_{1/2}$	0.08	2.87 (+12)	13.96	5.87 (+13)
$1s^2 2s 2p^6 3s 3p \ ^2P_{3/2}$	0.19	3.20 (+12)	13.94	4.10 (+13)
$1s^2 2s^2 2p^5 3s 4d \ ^4D_{1/2}$	0.12	5.11 (+12)	12.48	1.32 (+12)
$1s^2 2s^2 2p^5 3s 4d \ ^2P_{3/2}$	0.25	5.31 (+12)	12.46	1.20 (+12)
$1s^2 2s^2 2p^5 3s 4d \ ^4D_{3/2}$	0.29	6.38 (+12)	12.33	1.49 (+12)
$1s^2 2s^2 2p^5 3s 4d \ ^2P_{1/2}$	0.16	7.22 (+12)	12.33	1.51 (+12)
$1s^2 2s 2p^6 3s 4p \ ^2P_{3/2}$	0.05	1.35 (+12)	11.19	5.60 (+11)
$1s^2 2s 2p^6 3s 4p \ ^2P_{1/2}$	0.03	1.44 (+12)	11.19	5.02 (+11)

Table 3

Absorption oscillator strengths, wavelengths, radiative and autoionization probabilities

(from the ground level of Fe ¹⁴⁺)		$1s^2 2s^2 2p^6 3s^2 \ ^1S_0$			
to the upper level	f (abs)	A _r (s ⁻¹)	λ(Å)	A _a (s ⁻¹)	
$1s^2 2s^2 2p^5 3s^2 3d \ ^3D_1$	0.59	5.49 (+12)	15.51	7.75 (+12)	
$1s^2 2s^2 2p^5 3s^2 3d \ ^1P_1$	2.55	2.44 (+13)	15.26	1.43 (+13)	
$1s^2 2s 2p^6 3s^2 3p \ ^1P_1$	0.27	3.05 (+12)	14.09	8.99 (+13)	
$1s^2 2s^2 2p^5 3s^2 4d \ ^3D_1$	0.37	5.12 (+12)	12.74	8.49 (+12)	
$1s^2 2s^2 2p^5 3s^2 4d \ ^1P_1$	0.41	5.80 (+12)	12.60	8.78 (+12)	
$1s^2 2s 2p^6 3s^2 4p \ ^1P_1$	0.08	1.42 (+12)	11.38	8.82 (+13)	
(from the ground of Fe ⁸⁺)		$1s^2 2s^2 2p^6 3s^2 3p^6 \ ^1S_0$			
to the upper level	f (abs)	A _r (s ⁻¹)	λ(Å)	A _a (s ⁻¹)	
$1s^2 2s^2 2p^5 3s^2 3p^6 3d \ ^3D_1$	0.66	5.37 (+12)	16.59	4.19 (+14)	
$1s^2 2s^2 2p^5 3s^2 3p^6 3d \ ^1P_1$	1.52	1.27 (+13)	16.33	4.77 (+14)	
$1s^2 2s^2 2p^5 3s^2 3p^6 4d \ ^1P_1$	0.26	2.67 (+12)	14.59	4.05 (+14)	
$1s^2 2s^2 2p^5 3s^2 3p^6 4d \ ^3D_1$	0.18	1.89 (+12)	14.39	4.00 (+14)	
$1s^2 2s 2p^6 3s^2 3p^6 4p \ ^1P_1$	0.06	8.52 (+11)	12.80	6.20 (+13)	

Fig. 1. The *RGS* (*XMM-Newton*) first order spectrum of Seyfert 1 IRAS 13349+2438 corrected for cosmological redshift ($z = 0.10764$), from Sako et al. [5]. The wavelength bins are approximately 0.1 \AA wide. A best-fit model spectrum is superimposed in red.

Fig. 2. Effective-area-corrected, first-order (*XMM/RGS 1* (red) and (*XMM/RGS 2*) (blue)) first-order spectra of Seyfert 2 NGC 1068 shifted to its rest frame ($z = 0.00379$), from Kinkhabwala et al. [8]. The spectral discontinuities are due to chip gaps in the CCD arrays, bad pixels, etc.

Fig. 3. *Chandra/HETG* spectrum of Seyfert 1 NGC 3783 binned to 0.01 \AA focusing in the wavelength range $[15\text{-}18 \text{ \AA}]$ from Kaspi et al. [7]. Broad absorption feature from blended inner-shell 2p3d absorption lines of Fe ions.

Fig. 4. A schematic diagram of the Unified Scheme of AGN, from Urry & Padovani [12]. Surrounding the central supermassive black hole is a luminous accretion disk. The so-called “Broad Line Region” and “Narrow Line Region” produces broad lines and narrow lines observed in the optical range. The contour of the “Warm Absorber” observed in X-ray is also shown, as well as, jets only seen in Radio-Loud objects.

Fig. 5. Photo-absorption cross-sections of the different Fe ions (Fe^{+16} to Fe^{+6}) constituting the unresolved Fe-L feature, versus wavelengths. The final graph is built from the former graphs, assuming the same abundance for each ion.

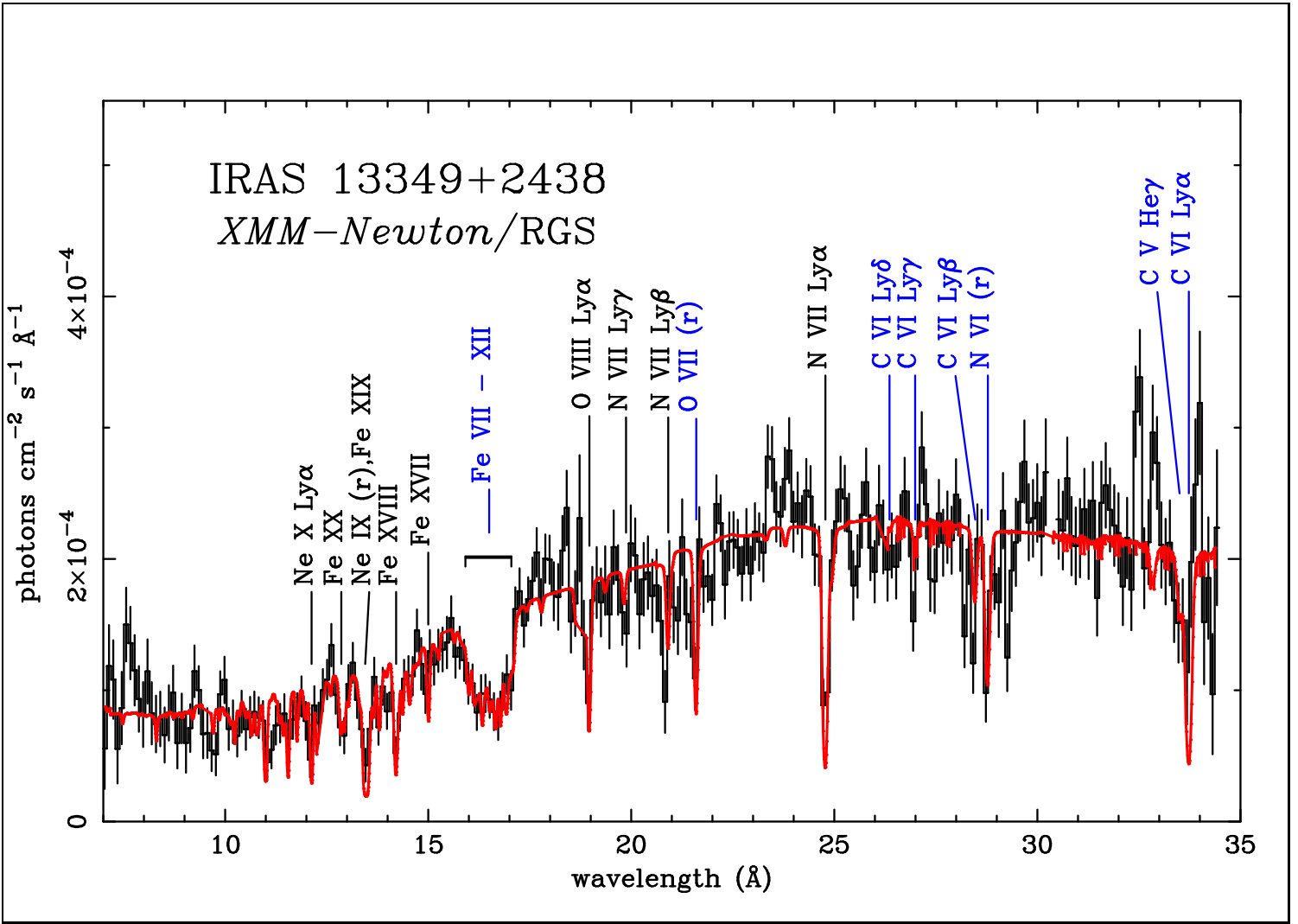


Figure 1

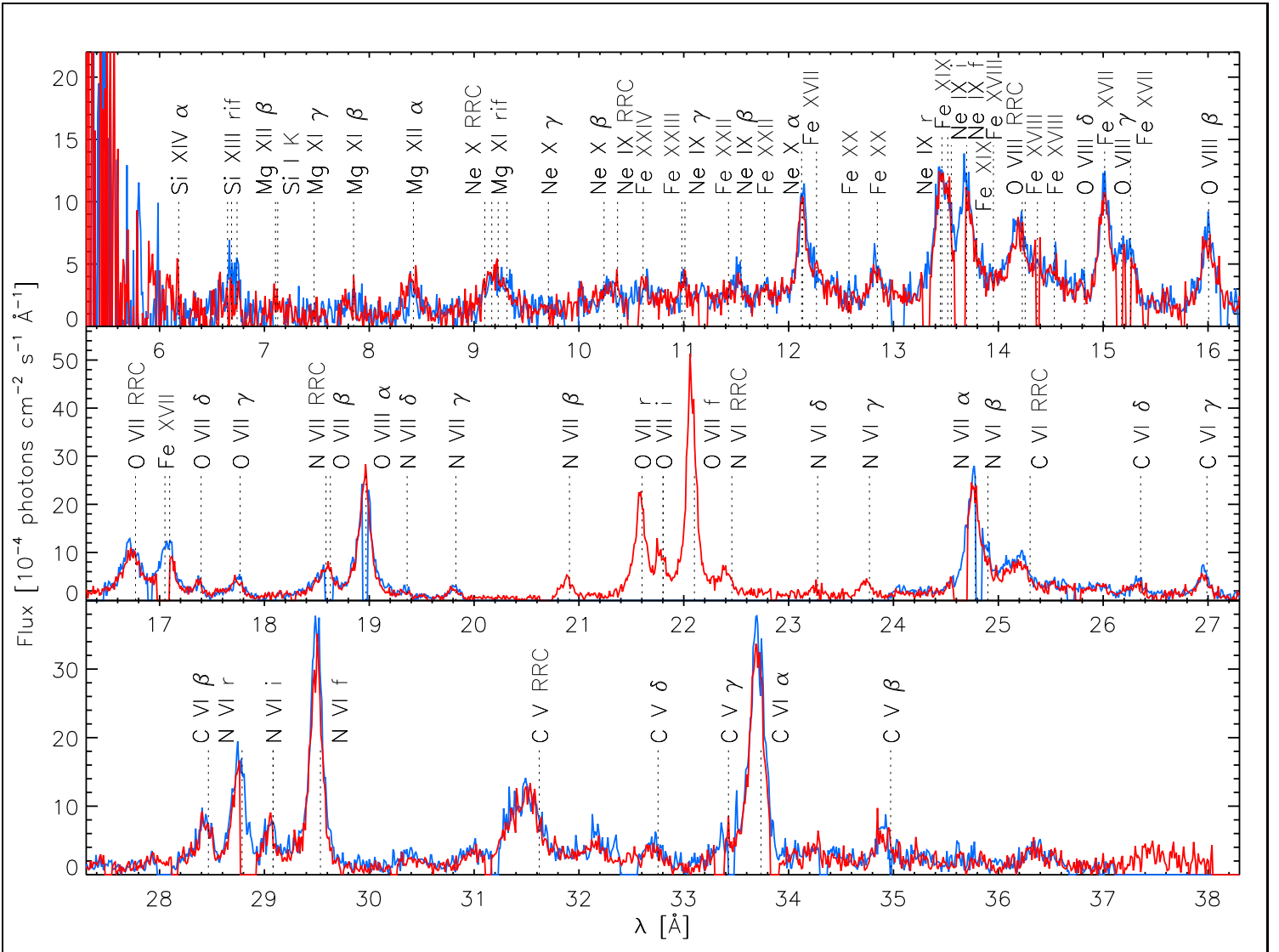


Figure 2

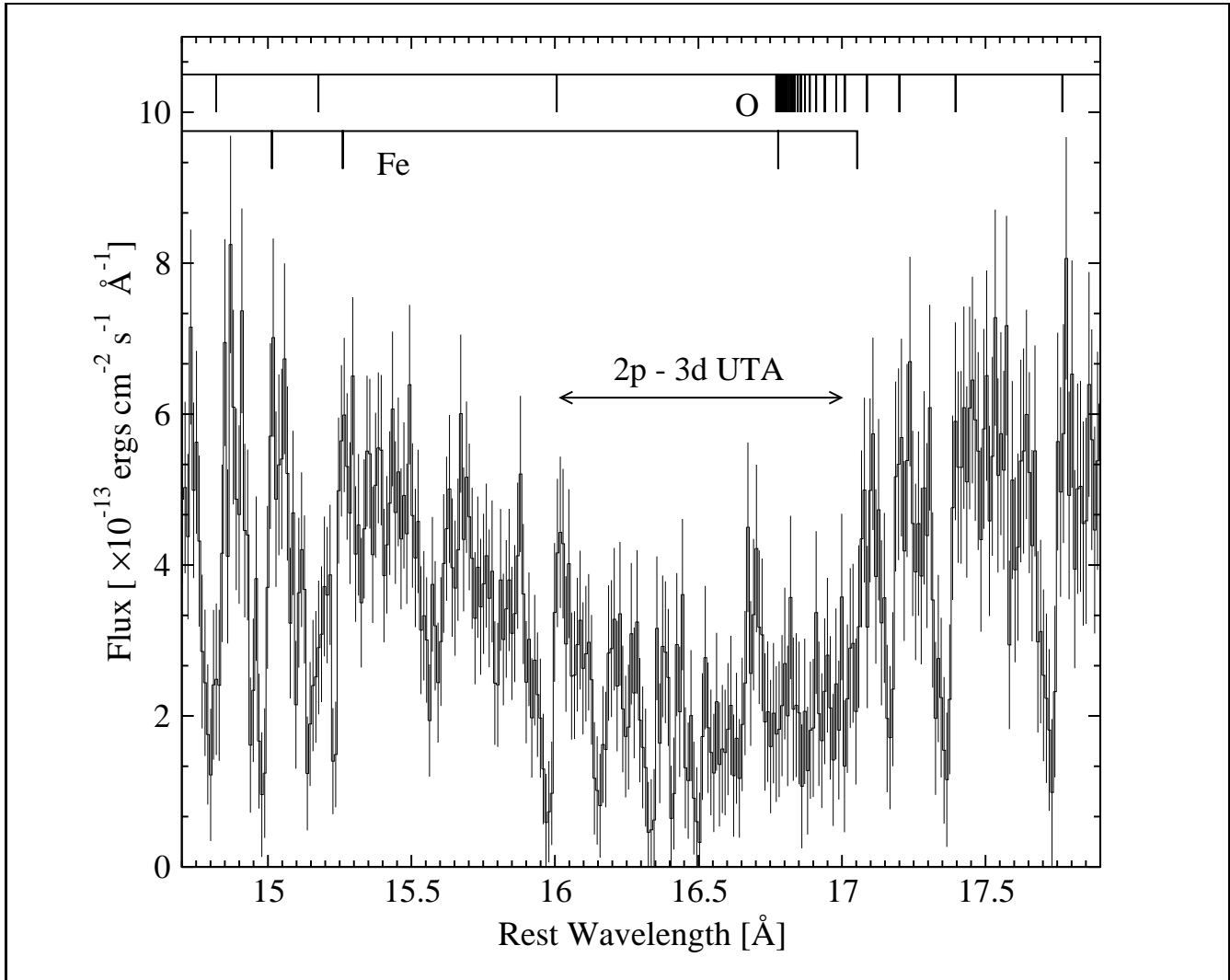


Figure 3

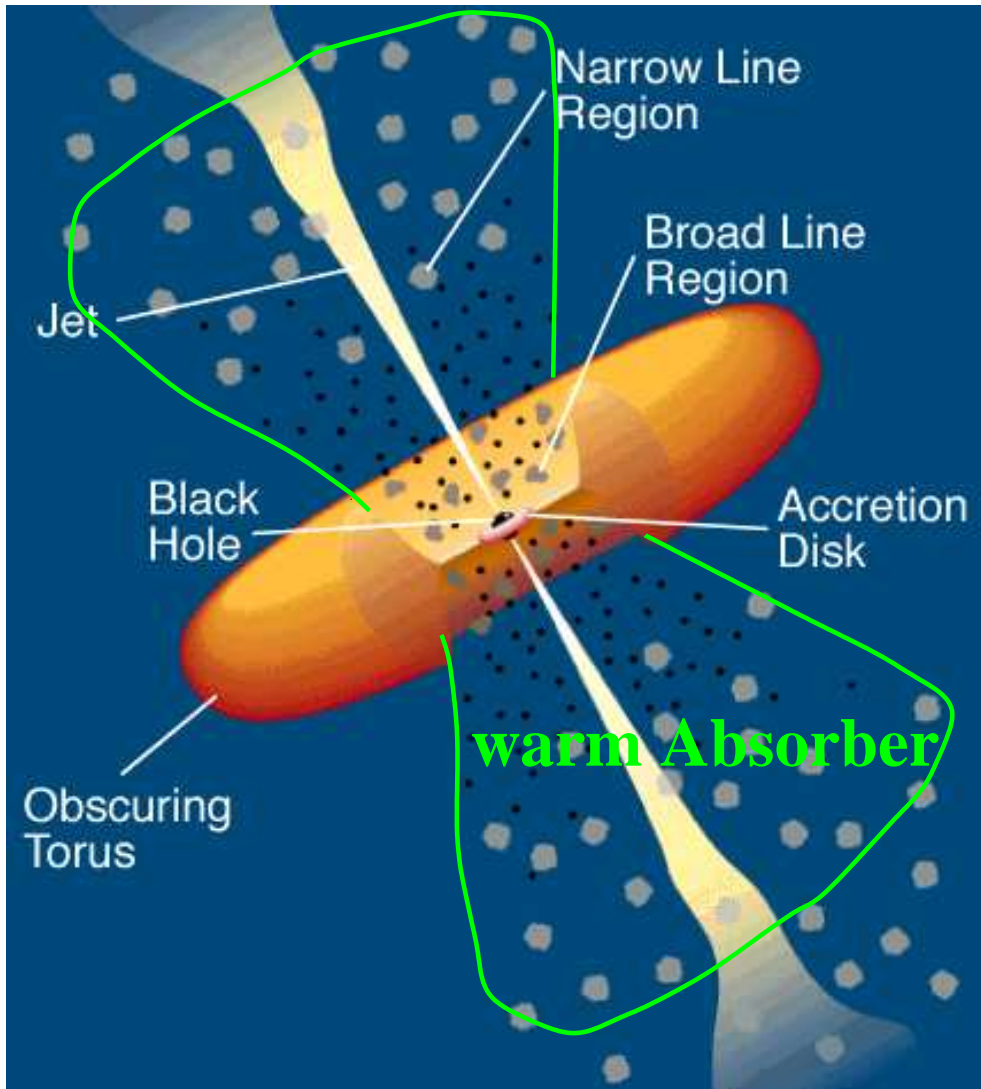


Figure 4

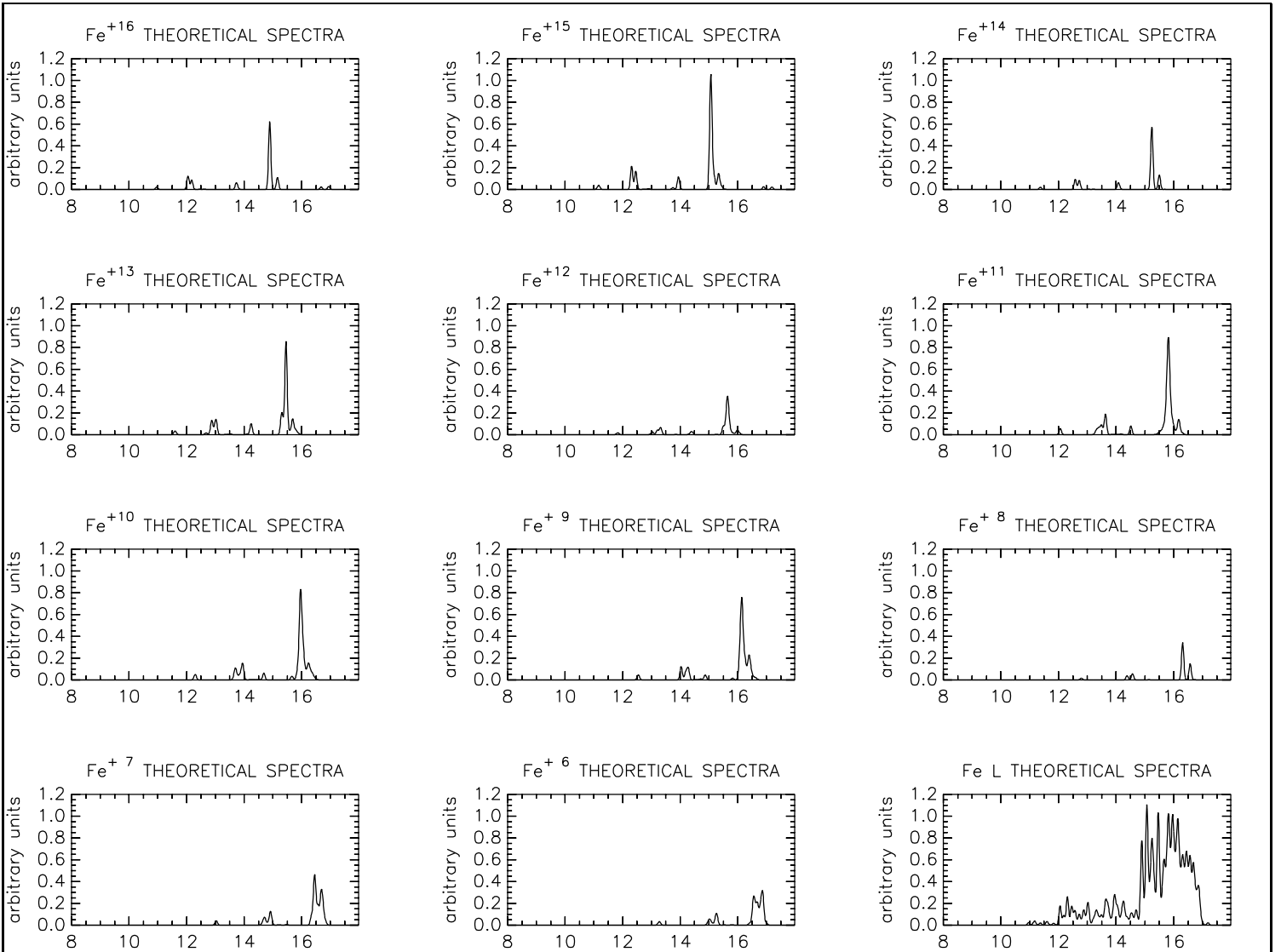


Figure 5